



Enhanced upconversion in one-dimensional photonic crystals: a simulation-based assessment within realistic material and fabrication constraints

CLARISSA L. M. HOFMANN,^{1,2,6,7} EMIL H. ERIKSEN,^{3,6,8} STEFAN FISCHER,⁴ BRYCE S. RICHARDS,^{2,5} PETER BALLING,³ AND JAN CHRISTOPH GOLDSCHMIDT¹

¹Fraunhofer Institute for Solar Energy Systems ISE, Heidenhofstrasse 2, 79110 Freiburg, Germany

²Institute of Microstructure Technology (IMT), Karlsruhe Institute of Technology, Hermann-von-Helmholtz-Platz 1, 76344 Eggenstein-Leopoldshafen, Germany

³Department of Physics and Astronomy, Aarhus University, Ny Munkegade 120, DK-8000 Aarhus C, Denmark

⁴Department of Chemistry, University of California - Berkeley, Berkeley, CA 94720, USA

⁵Light Technology Institute (LTI), Karlsruhe Institute of Technology (KIT), Engesserstrasse 13, 76131 Karlsruhe, Germany

⁶These authors contributed equally to this work

⁷clarissa.hofmann@ise.fraunhofer.de

⁸emher@au.dk

Abstract: This paper presents a simulation-based assessment of the potential for improving the upconversion efficiency of β -NaYF₄:Er³⁺ by embedding the upconverter in a one-dimensional photonic crystal. The considered family of structures consists of alternating quarter-wave layers of the upconverter material and a spacer material with a higher refractive index. The two photonic effects of the structures, a modified local energy density and a modified local density of optical states, are considered within a rate-equation-modeling framework, which describes the internal dynamics of the upconversion process. Optimal designs are identified, while taking into account production tolerances via Monte Carlo simulations. To determine the maximum upconversion efficiency across all realistically attainable structures, the refractive index of the spacer material is varied within the range of existing materials. Assuming a production tolerance of $\sigma = 1$ nm, the optimized structures enable more than 300-fold upconversion photoluminescence enhancements under one sun and upconversion quantum yields exceeding 15% under 30 suns concentration.

© 2018 Optical Society of America under the terms of the [OSA Open Access Publishing Agreement](#)

OCIS codes: (190.7220) Upconversion; (230.5298) Photonic crystals; (230.1480) Bragg reflectors; (160.5690) Rare-earth-doped materials; (240.0310) Thin films; (260.3800) Luminescence; (310.6628) Subwavelength structures, nanostructures; (310.6845) Thin film devices and applications.

References and links

1. D. Zhou, D. Liu, W. Xu, X. Chen, Z. Yin, X. Bai, B. Dong, L. Xu, and H. Song, "Synergistic upconversion enhancement induced by multiple physical effects and an angle-dependent anticounterfeit application," *Chem. Mater.* **29**, 6799–6809 (2017).
2. M. You, M. Lin, S. Wang, X. Wang, G. Zhang, Y. Hong, Y. Dong, G. Jin, and F. Xu, "Three-dimensional quick response code based on inkjet printing of upconversion fluorescent nanoparticles for drug anti-counterfeiting," *Nanoscale*. **8**, 10096–10104 (2016).
3. G. Gao, A. Turshatov, I. A. Howard, D. Busko, R. Joseph, D. Hudry, and B. S. Richards, "Up-conversion fluorescent labels for plastic recycling: a review," *Adv. Sustain. Syst.* **1**, 1600033 (2017).
4. P. Huang, W. Zheng, S. Zhou, D. Tu, Z. Chen, H. Zhu, R. Li, E. Ma, M. Huang, and X. Chen, "Lanthanide-doped LiLuF₄ upconversion nanoprobes for the detection of disease biomarkers," *Angewandte Chemie Int. Ed.* **53**, 1252–1257 (2014).

5. G. Chen, H. Qiu, P. N. Prasad, and X. Chen, "Upconversion nanoparticles: design, nanochemistry, and applications in theranostics," *Chem. Rev.* **114**, 5161–5214 (2014).
6. Y. Zhang, H. Hong, B. Sun, K. Carter, Y. Qin, W. Wei, D. Wang, M. Jeon, J. Geng, R. J. Nickles, G. Chen, P. N. Prasad, C. Kim, J. Xia, W. Cai, and J. F. Lovell, "Surfactant-stripped naphthalocyanines for multimodal tumor theranostics with upconversion guidance cream," *Nanoscale*, **9**, 3391–3398 (2017).
7. H. Qiao, Z. Cui, S. Yang, D. Ji, Y. Wang, Y. Yang, X. Han, Q. Fan, A. Qin, T. Wang, X.-P. He, W. Bu, and T. Tang, "Targeting osteocytes to attenuate early breast cancer bone metastasis by theranostic upconversion nanoparticles with responsive plumbagin release," *ACS Nano* **11**, 7259–7273 (2017).
8. T. Trupke, A. Shalav, B. Richards, P. Würfel, and M. Green, "Efficiency enhancement of solar cells by luminescent up-conversion of sunlight," *Sol. Energy Mater. Sol. Cells* **90**, 3327–3338 (2006).
9. B. S. Richards and A. Shalav, "Enhancing the near-infrared spectral response of silicon optoelectronic devices via up-conversion," *IEEE Trans. Electron Devices* **54**, 2679–2684 (2007).
10. X. Huang, S. Han, W. Huang, and X. Liu, "Enhancing solar cell efficiency: the search for luminescent materials as spectral converters," *Chem. Soc. Rev.* **42**, 173–201 (2013).
11. J. C. Goldschmidt and S. Fischer, "Upconversion for photovoltaics—a review of materials, devices and concepts for performance enhancement," *Adv. Opt. Mater.* **3**, 510–535 (2015).
12. W. Shockley and H. J. Queisser, "Detailed balance limit of efficiency of p-n junction solar cells," *J. Appl. Phys.* **32**, 510–519 (1961).
13. S. Fischer, E. Favilla, M. Tonelli, and J. C. Goldschmidt, "Record efficient upconverter solar cell devices with optimized bifacial silicon solar cells and monocrystalline BaY₂F₈:30% Er³⁺ upconverter," *Sol. Energy Mater. Sol. Cells* **136**, 127–134 (2015).
14. S. Fischer, J. Goldschmidt, P. Löper, G. Bauer, R. Brüggemann, K. Krämer, D. Biner, M. Hermle, and S. Glunz, "Enhancement of silicon solar cell efficiency by upconversion: optical and electrical characterization," *J. Appl. Phys.* **108**, 044912 (2010).
15. C. Strümpel, M. McCann, G. Beaucarne, V. Arkhipov, A. Slaoui, V. Švrček, C. Del Cañizo, and I. Tobias, "Modifying the solar spectrum to enhance silicon solar cell efficiency - an overview of available materials," *Sol. Energy Mater. Sol. Cells* **91**, 238–249 (2007).
16. K. W. Krämer, H. U. Güdel, and R. N. Schwartz, "Infrared-to-visible upconversion in LaCl₃:1% Er³⁺: energy-level and line-strength calculations," *Phys. Rev. B* **56**, 13830 (1997).
17. S. Fischer, A. Ivaturi, B. Fröhlich, M. Rüdiger, A. Richter, K. W. Krämer, B. S. Richards, and J. C. Goldschmidt, "Upconverter silicon solar cell devices for efficient utilization of sub-band-gap photons under concentrated solar radiation," *IEEE J. Photovolt.* **4**, 183–189 (2014).
18. S. K. W. MacDougall, A. Ivaturi, J. Marques-Hueso, K. W. Krämer, and B. S. Richards, "Broadband photoluminescent quantum yield optimisation of Er³⁺-doped β-NaYF₄ for upconversion in silicon solar cells," *Sol. Energy Mater. Sol. Cells* **128**, 18–26 (2014).
19. S. Fischer, B. Fröhlich, H. Steinkemper, K. W. Krämer, and J. C. Goldschmidt, "Absolute upconversion quantum yield of β-NaYF₄ doped with Er³⁺ and external quantum efficiency of upconverter solar cell devices under broad-band excitation considering spectral mismatch corrections," *Sol. Energy Mater. Sol. Cells* **122**, 197–207 (2014).
20. J.-C. Boyer and F. C. Van Veggel, "Absolute quantum yield measurements of colloidal NaYF₄:Er³⁺, Yb³⁺ upconverting nanoparticles," *Nanoscale* **2**, 1417–1419 (2010).
21. S. Fischer, R. Martín-Rodríguez, B. Fröhlich, K. W. Krämer, A. Meijerink, and J. C. Goldschmidt, "Upconversion quantum yield of Er³⁺-doped β-NaYF₄ and GdO₂S: the effects of host lattice, Er³⁺ doping, and excitation spectrum bandwidth," *J. Lumin.* **153**, 281–287 (2014).
22. K. W. Krämer, D. Biner, G. Frei, H. U. Güdel, M. P. Hehlen, and S. R. Lüthi, "Hexagonal sodium yttrium fluoride based green and blue emitting upconversion phosphors," *Chem. Mater.* **16**, 1244–1251 (2004).
23. M. Pollnau, D. Gamelin, S. Lüthi, H. Güdel, and M. Hehlen, "Power dependence of upconversion luminescence in lanthanide and transition-metal-ion systems," *Phys. Rev. B* **61**, 3337–3346 (2000).
24. I. Leonidov, V. Zubkov, A. Tyutyunnik, N. Tarakina, L. Surat, O. Koryakova, and E. Vovkotrub, "Upconversion luminescence in Er³⁺/Yb³⁺ codoped Y₂CaGe₄O₁₂," *J. Alloy. Compd.* **509**, 1339–1346 (2011).
25. S. Fischer, D. Kumar, F. Hallermann, G. V. Plessen, and C. Goldschmidt, "Enhanced upconversion quantum yield near spherical gold nanoparticles - a comprehensive simulation based analysis," *Opt. Express* **24**, A460–A475 (2016).
26. S. Fischer, F. Hallermann, T. Eichelkraut, G. V. Plessen, W. Karl, D. Biner, H. Steinkemper, M. Hermle, and J. C. Goldschmidt, "Plasmon enhanced upconversion luminescence near gold nanoparticles - simulation and analysis of the interactions," *Opt. Express* **20**, 271–282 (2012).
27. H. Mertens, A. F. Koenderink, and A. Polman, "Plasmon-enhanced luminescence near noble-metal nanospheres: comparison of exact theory and an improved gersten and nitzan model," *Phys. Rev. B* **76**, 115123 (2007).
28. S.-M. Lee, W. Li, P. Dhar, S. Malyk, Y. Wang, W. Lee, A. Benderskii, and J. Yoon, "High-performance flexible nanostructured silicon solar modules with plasmonically engineered upconversion medium," *Adv. Energy Mater.* **5**, 1500761 (2015).
29. H. Lakhotiya, A. Nazir, S. P. Madsen, J. Christiansen, E. Eriksen, J. Vester-Petersen, S. R. Johannsen, B. R. Jeppesen, P. Balling, A. N. Larsen, and B. Julsgaard, "Plasmonically enhanced upconversion of 1500 nm light via trivalent Er in a TiO₂ matrix," *Appl. Phys. Lett.* **109**, 263102 (2016).
30. E. Verhagen, L. Kuipers, and A. Polman, "Field enhancement in metallic subwavelength aperture arrays probed by

- erbium upconversion luminescence,” *Opt. Express* **17**, 14586–14598 (2009).
31. B. Herter, S. Wolf, S. Fischer, J. Gutmann, B. Bläsi, and J. C. Goldschmidt, “Increased upconversion quantum yield in photonic structures due to local field enhancement and modification of the local density of states - a simulation-based analysis,” *Opt. Express* **21**, A883–A900 (2013).
 32. C. L. M. Hofmann, B. Herter, S. Fischer, J. Gutmann, and J. C. Goldschmidt, “Upconversion in a Bragg structure: photonic effects of a modified local density of states and irradiance on luminescence and upconversion quantum yield,” *Opt. Express* **24**, 14895–14914 (2016).
 33. H. Wang, Z. Yin, W. Xu, D. Zhou, S. Cui, X. Chen, H. Cui, and H. Song, “Remarkable enhancement of upconversion luminescence on 2-D anodic aluminum oxide photonic crystals,” *Nanoscale* **8**, 10004–10009 (2016).
 34. C. Johnson, P. Reece, and G. Conibeer, “Theoretical and experimental evaluation of silicon photonic structures for enhanced erbium up-conversion luminescence,” *Sol. Energy Mater. Sol. Cells* **112**, 168–181 (2013).
 35. J. Liao, Z. Yang, J. Sun, S. Lai, B. Shao, J. Li, J. Qiu, Z. Song, and Y. Yang, “Preparation and upconversion emission modification of crystalline colloidal arrays and rare earth fluoride microcrystal composites,” *Sci. Reports* **5**, 7636 (2015).
 36. Z. Yin, Y. Zhu, W. Xu, J. Wang, S. Xu, B. Dong, L. Xu, S. Zhang, and H. Song, “Remarkable enhancement of upconversion fluorescence and confocal imaging of PMMA Opal/NaYF₄:Yb³⁺, Tm³⁺/Er³⁺ nanocrystals,” *Chem. Commun.* **49**, 3781–3783 (2013).
 37. S. Xu, W. Xu, Y. Wang, S. Zhang, Y. Zhu, L. Tao, L. Xia, P. Zhou, and H. Song, “NaYF₄:Yb,Tm nanocrystals and TiO₂ inverse opal composite films: a novel device for upconversion enhancement and solid-based sensing of avidin,” *Nanoscale* **6**, 5859–5870 (2014).
 38. W. Niu, L. T. Su, R. Chen, H. Chen, Y. Wang, A. Palaniappan, H. Sun, and A. I. Y. Tok, “3-dimensional photonic crystal surface enhanced upconversion emission for improved near-infrared photoresponse,” *Nanoscale* **6**, 817–824 (2014).
 39. Z.-X. Li, L.-L. Li, H.-P. Zhou, Q. Yuan, C. Chen, L.-D. Sun, and C.-H. Yan, “Colour modification action of an upconversion photonic crystal,” *Chem. Commun.* **43**, 6616–6618 (2009).
 40. F. Zhang, Y. Deng, Y. Shi, R. Zhang, and D. Zhao, “Photoluminescence modification in upconversion rare-earth fluoride nanocrystal array constructed photonic crystals,” *J. Mater. Chem.* **20**, 3895–3900 (2010).
 41. L. Tao, W. Xu, Y. Zhu, L. Xu, H. Zhu, Y. Liu, S. Xu, P. Zhou, and H. Song, “Modulation of upconversion luminescence in Er³⁺, Yb³⁺-codoped lanthanide oxyfluoride (YOF, GdOF, LaOF) inverse opals,” *J. Mater. Chem. C* **2**, 4186–4195 (2014).
 42. Y. Yang, P. Zhou, W. Xu, S. Xu, Y. Jiang, X. Chen, and H. Song, “NaYF₄:Yb³⁺, Tm³⁺ inverse opal photonic crystals and NaYF₄:Yb³⁺, Tm³⁺/TiO₂ composites: synthesis, highly improved upconversion properties and NIR photoelectric response,” *J. Mater. Chem. C* **4**, 659–662 (2016).
 43. J. H. Lin, H. Y. Liou, C.-D. Wang, C.-Y. Tseng, C.-T. Lee, C.-C. Ting, H.-C. Kan, and C. C. Hsu, “Giant enhancement of upconversion fluorescence of NaYF₄:Yb³⁺, Tm³⁺ nanocrystals with resonant waveguide grating substrate,” *ACS Photonics* **2**, 530–536 (2015).
 44. Z. Yin, H. Li, W. Xu, S. Cui, D. Zhou, X. Chen, Y. Zhu, G. Qin, and H. Song, “Local field modulation induced three-order upconversion enhancement: combining surface plasmon effect and photonic crystal effect,” *Adv. Mater.* **28**, 2518–2525 (2016).
 45. B. Shao, Z. Yang, J. Li, J. Yang, Y. Wang, J. Qiu, and Z. Song, “Au nanoparticles embedded inverse opal photonic crystals as substrates for upconversion emission enhancement,” *J. Am. Ceram. Soc.* **100**, 988–997 (2017).
 46. S. Fischer, H. Steinkemper, P. Löper, M. Hermle, and J. C. Goldschmidt, “Modeling upconversion of erbium doped microcrystals based on experimentally determined Einstein coefficients,” *J. Appl. Phys.* **111**, 13109 (2012).
 47. C. L. M. Hofmann, S. Fischer, C. Reitz, B. S. Richards, and J. C. Goldschmidt, “Comprehensive analysis of photonic effects on up-conversion of β -NaYF₄:Er³⁺ nanoparticles in an organic-inorganic hybrid 1D photonic crystal,” *Proc. SPIE* **9885**, 99851(2016).
 48. R. E. Thoma, H. Insley, and G. M. Hebert, “The sodium fluoride-tanthanide trifluoride systems,” *Inorg. Chem.* **5**, 1222–1229 (1966).
 49. L. M. Goldenberg, V. Lisinetskii, and S. Schrader, “Fast and simple fabrication of organic bragg mirrors—application to plastic microchip lasers,” *Laser Phys. Lett.* **10**, 055808 (2013).
 50. A. Mereuta, A. Sirbu, A. Caliman, G. Suruceanu, V. Iakovlev, Z. Mickovic, and E. Kapon, “Fabrication and performance of 1.3- μ m 10-Gb/s CWDM wafer-fused VCSELs grown by MOVPE,” *J. Cryst. Growth* **414**, 210–214 (2015).
 51. R. L. Puurunen, J. Saarihtä, and H. Kattelus, “Implementing ALD layers in MEMS processing,” *ECS Transactions* **11**, 3–14 (2007).
 52. C. L. Mitsas and D. I. Siapkas, “Generalized matrix method for analysis of coherent and incoherent reflectance and transmittance of multilayer structures with rough surfaces, interfaces, and finite substrates,” *Appl. Opt.* **34**, 1678–1683 (1995).
 53. S. G. Johnson and J. D. Joannopoulos, “Block-iterative frequency-domain methods for Maxwell’s equations in a planewave basis,” *Opt. Express* **8**, 173–190 (2001).
 54. M. Barth, A. Gruber, and F. Cichos, “Spectral and angular redistribution of photoluminescence near a photonic stop band,” *Phys. Rev. B* **72**, 085129 (2005).
 55. S. John and K. Busch, “Photonic bandgap formation and tunability in certain self-organizing systems,” *J. Light.*

- Technol. **17**, 1931 (1999).
56. J. M. Bendickson, J. P. Dowling, and M. Scalora, "Analytic expressions for the electromagnetic mode density in finite, one-dimensional, photonic band-gap structures," *Phys. Rev. E* **53**, 4107–4121 (1996).
 57. E. Yeganeh, A. Lagendijk, A. P. Mosk, and W. L. Vos, "Local density of optical states in the band gap of a finite one-dimensional photonic crystal," *Phys. Rev. B* **89**, 045123 (2014).
 58. J. Gutmann, H. Zappe, and J. C. Goldschmidt, "Quantitative modeling of fluorescent emission in photonic crystals," *Phys. Rev. B* **88**, 205118 (2013).
 59. J. Gutmann, "Photonic luminescent solar concentrators," Ph.D. thesis, Albert-Ludwigs University Freiburg, Technical Faculty (2014).
 60. J. P. Dowling and C. M. Bowden, "Atomic emission rates in inhomogeneous media with applications to photonic band structures," *Phys. Rev. A* **46**, 612 (1992).
 61. M. De Dood, J. Knoester, A. Tip, and A. Polman, "Förster transfer and the local optical density of states in erbium-doped silica," *Phys. Rev. B* **71**, 115102 (2005).
 62. C. Blum, N. Zijlstra, A. Lagendijk, M. Wubs, A. P. Mosk, V. Subramaniam, and W. L. Vos, "Nanophotonic control of the Förster resonance energy transfer efficiency," *Phys. Rev. Lett.* **109**, 203601 (2012).
 63. P. Andrew and W. L. Barnes, "Förster energy transfer in an optical microcavity," *Science*. **290**, 785–788 (2000).
 64. F. T. Rabouw, S. A. Den Hartog, T. Senden, and A. Meijerink, "Photonic effects on the Förster resonance energy transfer efficiency," *Nat. Commun.* **5**, 3610 (2014).
 65. C. M. Johnson, P. J. Reece, and G. J. Conibeer, "Slow-light-enhanced upconversion for photovoltaic applications in one-dimensional photonic crystals," *Opt. Lett.* **36**, 3990–3992 (2011).
 66. T. F. Krauss, "Slow light in photonic crystal waveguides," *J. Phys. D: Appl. Phys.* **40**, 2666 (2007).
 67. J. C. Goldschmidt, P. Loper, S. Fischer, S. Janz, M. Peters, S. W. Glunz, G. Willeke, E. Lifshitz, K. Kramer, and D. Biner, "Advanced upconverter systems with spectral and geometric concentration for high upconversion efficiencies," in *Conference on Optoelectronic and Microelectronic Materials and Devices* (IEEE, 2008), pp. 307–311.

1. Introduction

Upconversion (UC) is the process of converting two (or more) photons into one photon of higher energy. It is relevant in a broad range of applications, from anti counterfeiting [1, 2], plastic recycling [3], bioimaging [4, 5] and theranostics [5–7] to photovoltaics [8–11]. In photovoltaics, UC enables the utilization of sub-bandgap photons, which for silicon-based solar cells raises the theoretical efficiency limit from $\approx 30\%$ [12] to $\approx 40\%$ [8]. Spectrally suitable materials capable of harvesting near-infrared light have been identified among the trivalent rare-earth materials, in particular the Er^{3+} ion [9, 13–16]. In this study, we consider erbium-doped hexagonal sodium yttrium fluoride ($\beta\text{-NaYF}_4\text{:Er}^{3+}$), which ranges among the best performing materials for UC applications in the context of silicon-based photovoltaics [17–22]. However, even for this material system, the UC efficiency remains too low for commercial exploitation [11].

UC is a multi-photon process and thus of non-linear nature [23]. For UC to take place, it requires that at least two photons are absorbed in a small volume within a short period of time. Therefore, in the unsaturated regime, to which non-concentrated solar illumination belongs [24], the UC efficiency can be increased by light concentration. Besides focusing by conventional means, such as lenses, strong local field enhancements can be achieved through plasmonic structures [25–30]. The strong field leads to an increased excitation density in the upconverter and consequently to a higher UC efficiency. A major drawback of plasmonic structures, however, is parasitic absorption, which reduces the energy density of the incident field available for upconversion. Furthermore, additional non-radiative loss channels are introduced, which can dissipate energy from the excited upconverter ions. In the immediate vicinity of plasmonic structures, the non-radiative losses strongly reduce the UC emission, which is particularly problematic as it is typically here the maximum field enhancement occurs [25, 26]. Another way to obtain strong local field enhancements is through dielectric photonic structures [31–41]. Unlike plasmonic structures, photonic structures do not inherently suffer from parasitic absorption, but they do modify the local density of optical states (LDOS). As the LDOS affects the probability of spontaneous emission, a modified LDOS can potentially increase UC emission and/or suppress loss channels, all of which can be tailored through structural engineering [31, 32].

The literature on the application of photonic crystals to improve UC luminescence is dominated

by inverse opal [37,40–42] and opal structures [36,38]. For those structures, an experimentally measured UC luminescence enhancements of up to 43 times has been reported [37]. Moreover, a very high UC luminescence enhancement of 10^4 has been reported for a waveguide structure [43]. Recently, photonic-plasmonic hybrid structures have been experimentally demonstrated, yielding UC luminescence enhancement factors up to three orders of magnitude [44,45]. Additionally, an experimental study of one-dimensional photonic crystals was carried out by [34], where the crystal was formed from Er^{3+} -doped porous silicon with the periodic variation of the refractive index obtained by varying the silicon porosity. In that case, a maximum UC luminescence enhancement of a factor of 26.6 was reported.

In most studies, the design of the photonic structure is not optimized, but simply chosen such that the excitation lies at the photonic band edge [36–38]. In a few reports the actual local field is simulated, based on which an optimal design is realized [33,34,43,44]. However, the effect of the LDOS and the dynamics of the UC process are rarely considered. To address this issue, a rate-equation-modeling framework has been developed as part of our previous work. The model considers the combined effects of the modified LDOS and the modified local energy density [31,32,46]. In a theoretical study of the photonic effects on UC, it has been demonstrated that it is indeed important to include the effect of the modified LDOS [32]. Furthermore, the so-called Bragg structure was identified as a promising design for increasing UC efficiency [32,47]. In contrast to structures that exploit surface effects, the amount of upconverter material in a Bragg structure can be increased by adding more layers in the design. In applications, this is a very important property, in particular for the weakly-absorbing rare-earth materials.

In this work, we present a simulation-based assessment of the potential of the Bragg structure for increasing the UC efficiency of 1523 nm excitation light via the use of $\beta\text{-NaYF}_4\text{:Er}^{3+}$ nanophosphors. The Bragg structure consists of alternating quarter-wave layers of two materials with refractive indices n_{low} and n_{high} , with respect to a design wavelength $\lambda_D = 4nd$, where d is the layer thickness and n the refractive index, as shown in Fig. 1(a). The outer-most layers

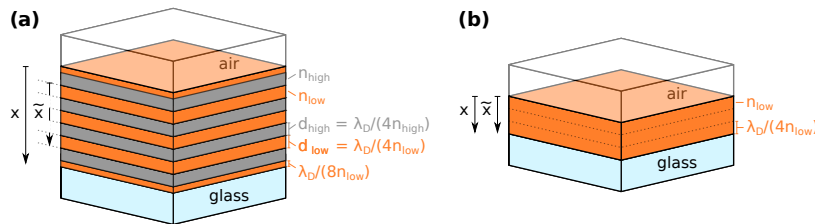


Fig. 1. Structural sketches of the Bragg structure (a) and the reference structure (b). The Bragg structure consists of alternating quarter-wave layers, with respect to a design wavelength λ_D , of an active and a spacer material with refractive indices n_{low} and n_{high} . The outermost layers have a reduced optical thickness of $\lambda_D/(8n)$ and are assumed passive. The reference structure consists of a single, homogeneous layer containing the same amount of active material as the corresponding Bragg structure.

have a reduced optical thickness of only $\lambda_D/(8n)$, which enables a more efficient in-coupling of broad-band excitation. In principle, the upconverting material could be embedded in either layer. However, to avoid scattering, which would cause decoherence and thus suppress the desired photonic effects, the upconverting material must be index-matched with respect to the host layer. Since the refractive index of $\beta\text{-NaYF}_4\text{:Er}^{3+}$ (≈ 1.5 [48]) is relatively low, choosing it as the high index layer would allow only for a very low refractive index contrast. Therefore, we choose the low index layers as the active ones, containing the upconverter material, thus fixing $n_{\text{low}} = 1.5$. The outer-most layers of reduced thickness are assumed passive, but feature the same refractive index as n_{low} . The spacer material can in principle be chosen freely with the only constraint that the absorption should be low within the spectral region of interest. To accommodate all materials,

we consider the range $1.5 < n_{\text{high}} \leq 4.0$. Examples of high refractive index materials that remain transparent in the region of the main UC emission include TiO_2 and a-Si:H. As the reference, we choose a homogeneous structure with refractive index n_{low} , containing the same amount of active material as the corresponding Bragg structure, see Fig. 1(b).

While ideal photonic crystals are infinite and perfectly periodic, the experimental realizations are finite and suffer from production imperfections. As demonstrated previously [32], the beneficial peak in the energy density enhancement is very narrow in λ_D , or equivalently the layer thickness, implying a high sensitivity to fabrication tolerances. For production of Bragg-like structures a variety of thin film fabrication methods are available. A fast and efficient production method is spin-coating from solution. With this process, layer uniformities of 1-2% of the total layer thickness can be achieved [49]. Higher layer uniformities can be reached in chemical vapour deposition processes. Using metalorganic vapour phase epitaxy (MOVPE), a layer thickness control of 0.1-0.5% has been reported [50]. Another high-precision production method is atomic layer deposition (ALD), where a thickness accuracy of 0.5% is possible for TiO_2 thin films at deposition temperatures above 250°C [51]. To enable a realistic assessment of the performance of fabricated structures in this work, we take into account finite production tolerances via Monte Carlo simulations. Based on achieved thickness control of 0.5% reported in the literature [50, 51], a realistic target tolerance of 0.5% is assumed in the main analysis of this work, which corresponds to an absolute value of ≈ 1 nm. We choose a value at the limit of what is currently possible, imagining that such accuracy will be enabled in routine production by future advances in nanofabrication techniques. One option could be, for example, to produce the whole layer stack with ALD processes.

We first present the methods for evaluating the local energy density, including the Monte Carlo method, in Section 2.1, after which the LDOS calculations are introduced in Section 2.2. The photonic effects are coupled via a rate equation model (REM), presented in Section 2.3, which yields the upconversion quantum yield (UCQY) and the upconversion photoluminescence (UCPL). The potential for increasing the local energy density, assuming different production accuracies, is investigated in Section 3.1, while the modified LDOS is discussed in Section 3.2. Finally, in Section 3.3, we present the calculated UCQY and UCPL enhancements, scanning through all design parameters. Additionally, different irradiance regimes, targeting different application scenarios, are considered.

2. Methods

2.1. Local energy density

For stacks of planar, homogeneous layers an analytical solution for the electrical field distribution, $\mathbf{E}(x)$, exists. It can be found efficiently using the transfer matrix method [52] from which the local energy density of the electric field, $u(x)$, can be calculated as

$$u(x) = \frac{1}{2} \varepsilon(x) |\mathbf{E}(x)|^2. \quad (1)$$

We define the relative local energy density as

$$u_{\text{rel}}(\tilde{x}) = \frac{u_{\text{brg}}(\tilde{x})}{u_{\text{ref}}(\tilde{x})}, \quad (2)$$

where for the Bragg structure the \tilde{x} coordinate runs inside the active layers only, as indicated in Fig. 1. For visualization purposes we define also the average relative energy density

$$\bar{u}_{\text{rel}} = \frac{\int u_{\text{brg}}(\tilde{x}) d\tilde{x}}{\int u_{\text{ref}}(\tilde{x}) d\tilde{x}}. \quad (3)$$

To account for final production tolerances, Monte Carlo simulations are carried out. A number of calculations are performed where for each layer the thickness d is modified as

$$d \rightarrow d + \delta d, \quad (4)$$

where δd is drawn from a Gaussian distribution with a standard deviation σ representing the production accuracy. Finally, the energy density is determined from the (incoherent) average across all calculations.

2.2. Local density of optical states

For infinite periodic structures, i.e. ideal photonic crystals, the local density of optical states (LDOS) can be derived from eigenmode calculations [53–55]. In this work, we use the MIT Photonic bands [53] software package. While the ideal crystal assumption is not accurate for Bragg structures with only a small number of layers [56,57], the structures of main interest in this work have 10 active layers or more. Additionally, the eigenmode approach is relevant in a future perspective, as it permits calculation of an angularly resolved LDOS [58], which is important for our future work on the modified directionality of upconversion (UC) emission in a Bragg structure.

Due to the scale invariance of the problem, we consider dimensionless quantities

$$\mathbf{k}' = \frac{\mathbf{k}a}{2\pi}, \quad \omega' = \frac{\omega a n}{2\pi c_0}, \quad (5)$$

where \mathbf{k} is the wave vector, a the size of the Wigner-Seitz unit cell and c_0 the speed of light in vacuum. For a given eigenvector \mathbf{k}'_j , an eigenmode calculation yields the mode frequency $\omega'_{b,\mathbf{k}'_j}$ and the electric field profile $\mathbf{E}_{b,\mathbf{k}'_j}(x)$ with b being the band index. Applying the histogramming method and exploiting the in-plane symmetry of the Bragg structure [58], the quasi-three-dimensional LDOS can be calculated as

$$\text{LDOS}(x, \omega') = \sum_b \sum_{\mathbf{k}' \in \mathbf{K}_{b,\omega'}} |\mathbf{E}_{b,\mathbf{k}'}(x)|^2 \cdot 2\pi k'_y \quad (6)$$

$$\text{with } \mathbf{K}_{b,\omega'} = \{\mathbf{k}'_j | \omega' \leq \omega_{b,\mathbf{k}'_j} \leq \omega' + \Delta\omega'\},$$

where \mathbf{k}'_j is sampled on an equidistant grid with spacing $\Delta k'$ in the first quadrant of the xy -plane in reciprocal space. While the sampling in the x -direction is bound by the edge of the First Brillouin Zone at $k'_x = 0.5$, k'_y is unbound due to the lack of translational symmetry. In this work, all modes across the first seven bands in the range $0 < \omega' < 1.4$ were calculated. To obtain all contributing modes for the relevant emission frequencies and material combinations, the range $0 \leq k'_y \leq 5.4$ was considered. An optional output in MIT Photonic bands is the electric field energy density, from which the squared amplitude of the electric field can be computed,

$$|\mathbf{E}_{b,\mathbf{k}'}(x)|^2 = \frac{2u_{b,\mathbf{k}'}(x)}{\varepsilon(x)}. \quad (7)$$

Subsequently, the LDOS can be calculated according to Eq. (6). Across all calculations presented in this work, discretization steps of $\Delta k' = 10^{-3}$ and $\Delta\omega' = 10^{-3}$ were used. The limited resolution in k -space caused a significant amount of binning noise. To reduce the noise, the LDOS was smoothed along the frequency axis using a Gaussian filter with $\sigma = 5$.

As the reference is homogeneous, the LDOS is independent of the position. Hence, it is equal to the DOS up to a multiplicative constant which depends on the discretization of the Wigner-Seitz unit cell. The DOS for a homogeneous medium has an analytical form [59],

$$\text{DOS3D}(\omega') = \frac{4\pi n^3}{\Delta k'^2} \omega'^2. \quad (8)$$

Applying the same binning procedure as in the numerical calculation for the Bragg structure, the binned reference LDOS can be calculated as

$$\text{LDOS}_{\text{ref}}(\omega') = \int_{\omega'}^{\omega'+\Delta\omega'} \text{DOS3D}(\omega'') d\omega'' = \frac{4\pi n^3 \Delta\omega'}{\Delta k'^2} \left(\omega'^2 + \omega' \Delta\omega + \frac{\Delta\omega^2}{3} \right) \quad (9)$$

with $n = n_{\text{low}}$ [58]. We define the relative LDOS in the Wigner-Seitz unit cell as

$$\text{LDOS}_{\text{rel}}(x, \omega') = \frac{\text{LDOS}_{\text{brg}}(x, \omega')}{\text{LDOS}_{\text{ref}}(\omega')}. \quad (10)$$

For visualization purposes we define also the average relative LDOS across the active layers of the Bragg structure,

$$\overline{\text{LDOS}}_{\text{rel}}(\omega') = \frac{\int \text{LDOS}_{\text{brg}}(\tilde{x}, \omega') d\tilde{x}}{\int \text{LDOS}_{\text{ref}}(\omega') d\tilde{x}}. \quad (11)$$

The relative LDOS for a particular transition $i \rightarrow f$ and design, characterized by λ_{fi} and λ_D , respectively, is mapped to the dimensionless transition frequency ω'_{fi} as [32]

$$\omega'_{fi} = \frac{n_{\text{low}} + n_{\text{high}}}{4n_{\text{low}}n_{\text{high}}} \frac{\lambda_D}{\lambda_{fi}}. \quad (12)$$

2.3. Rate equation model

We describe the dynamics of the UC process using a modified version of a rate equation model (REM) originally developed for homogeneous media [46]. All experimental parameters are measured for an excitation wavelength of 1523 nm, for which the main UC emission lies at 984 nm. The first seven energy levels of $\beta\text{-NaYF}_4:\text{Er}^{3+}$, shown in Fig. 2, are considered. The energy levels

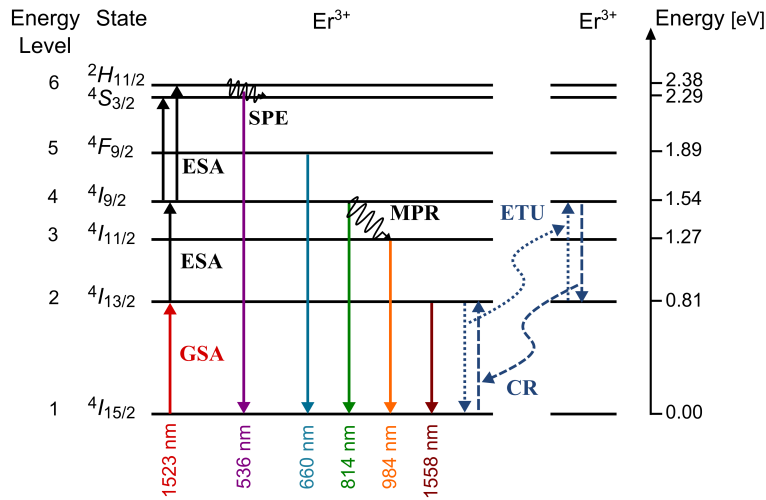


Fig. 2. Schematic of the first seven energy levels in $\beta\text{-NaYF}_4:\text{Er}^{3+}$ included in the rate equation model, along with most important transitions for the UC process. The highest two energy levels are treated as one due to their close proximity. For the considered excitation of 1523 nm wavelength, the main UC emission lies at 984 nm.

of the $2H_{11/2}$ and the $2S_{3/2}$ states are treated as one effective energy level, due to their close proximity. The occupation of each level is described as an element of the occupation density vector

n. The linear processes included in the REM are ground state absorption (GSA), excited state absorption (ESA), stimulated emission (STE), spontaneous emission (SPE) and multi-phonon relaxation (MPR). Additionally, the non-linear Förster energy transfer processes, energy transfer upconversion (ETU) and cross relaxation (CR), are considered. The most important processes are indicated in Fig. 2. The rate of change of the occupation density vector yields

$$\dot{\mathbf{n}} = [M_{\text{GSA}} + M_{\text{ESA}} + M_{\text{STE}} + M_{\text{SPE}} + M_{\text{MPR}}] \mathbf{n} + \mathbf{v}_{\text{ETU}}(\mathbf{n}) + \mathbf{v}_{\text{CR}}(\mathbf{n}), \quad (13)$$

where M denotes transition matrices and \mathbf{v} vector functions. Additional details on the REM for the case of a homogeneous medium are available in the original work [46].

The modifications of the REM due to the changes in the photonic environment imposed by the photonic structure have been developed in [31]. The probability for stimulated processes, i.e. absorption and stimulated emission, depends linearly on the local energy density $u(x, \omega'_{fi})$

$$W_{fi} = \frac{\pi^2 c_0^3}{\hbar \omega'_{fi}} \frac{g_f}{g_i} u(x, \omega'_{fi}) A_{fi} \propto u(x, \omega'_{fi}), \quad (14)$$

where c_0 is the speed of light, g_f and g_i the degeneracies of the final and initial states, respectively, and A_{fi} the Einstein coefficient of spontaneous emission. The change in local energy density due to the photonic structure can thus be taken into account by scaling the corresponding transition matrices by the relative local energy density

$$M_{\text{GSA}} \rightarrow M_{\text{GSA}} u_{\text{rel}}(x, \omega'_{fi}), \quad M_{\text{ESA}} \rightarrow M_{\text{ESA}} u_{\text{rel}}(x, \omega'_{fi}), \quad M_{\text{STE}} \rightarrow M_{\text{STE}} u_{\text{rel}}(x, \omega'_{fi}). \quad (15)$$

The spontaneous emission probability P_{fi} is governed by Fermi's golden rule [60]

$$P_{fi} = \frac{2\pi}{\hbar} |\langle f | H_{\text{int}} | i \rangle|^2 \text{LDOS}(x, \omega'_{fi}) \propto \text{LDOS}(x, \omega'_{fi}), \quad (16)$$

where H_{int} is the interaction Hamiltonian between initial, $|i\rangle$, and final, $|f\rangle$, electronic states. To incorporate the effect of the modified LDOS into the REM, the Einstein coefficients for spontaneous emission are scaled as

$$A_{fi} \rightarrow A_{fi} \text{LDOS}_{\text{rel}}(x, \omega'_{fi}). \quad (17)$$

It remains a subject of discussion in the literature whether Förster energy transfer processes, which are crucial to the UC process in lanthanide-doped materials, are also influenced by changes in the local photonic environment [61–63]. In this work we follow the arguments of [61, 64] and neglect any such effects.

The output of the REM is a steady-state occupation density vector \mathbf{N} from which the main figures of merit, the upconversion photoluminescence (UCPL) and the internal upconversion quantum yield (UCQY), can be calculated. The photoluminescence (PL) for each transition is

$$\text{PL}_{fi} = \int A_{fi}(x) N_i(x) dx \quad (18)$$

where N_i is the steady-state occupation density of level i . The energy level numbering scheme is shown in Fig. 2. In the UCPL, we consider only the main UC emission of the $3 \rightarrow 1$ transition,

$$\text{UCPL} = \text{PL}_{31}. \quad (19)$$

This approximation enables a simpler analysis going forward, and the associated error is small, as the $3 \rightarrow 1$ transition accounts for more than 95% of the emitted, upconverted photons. To obtain the UCQY, the UCPL is divided by the number of absorbed photons,

$$\text{UCQY} = \frac{\text{UCPL}}{N_1 M_{\text{GSA},12} + N_2 M_{\text{ESA},24} + N_4 M_{\text{ESA},46}}. \quad (20)$$

To enable clear visualization of the effect of the Bragg structure, we define also the relative UCPL

$$\text{UCPL}_{\text{rel}} = \frac{\text{UCPL}_{\text{brg}}}{\text{UCPL}_{\text{ref}}}. \quad (21)$$

3. Results

3.1. Local energy density

The average relative energy density, \bar{u}_{rel} , for an exemplary Bragg structure with $n_{\text{high}} = 2.3$ and a number of active UC layers ($\#_{\text{al}}$) of 25 is plotted in Fig. 3(a) for normal incidence and monochromatic excitation at $\lambda_{\text{exc}} = 1523$ nm in dependence on the design wavelength λ_D . An

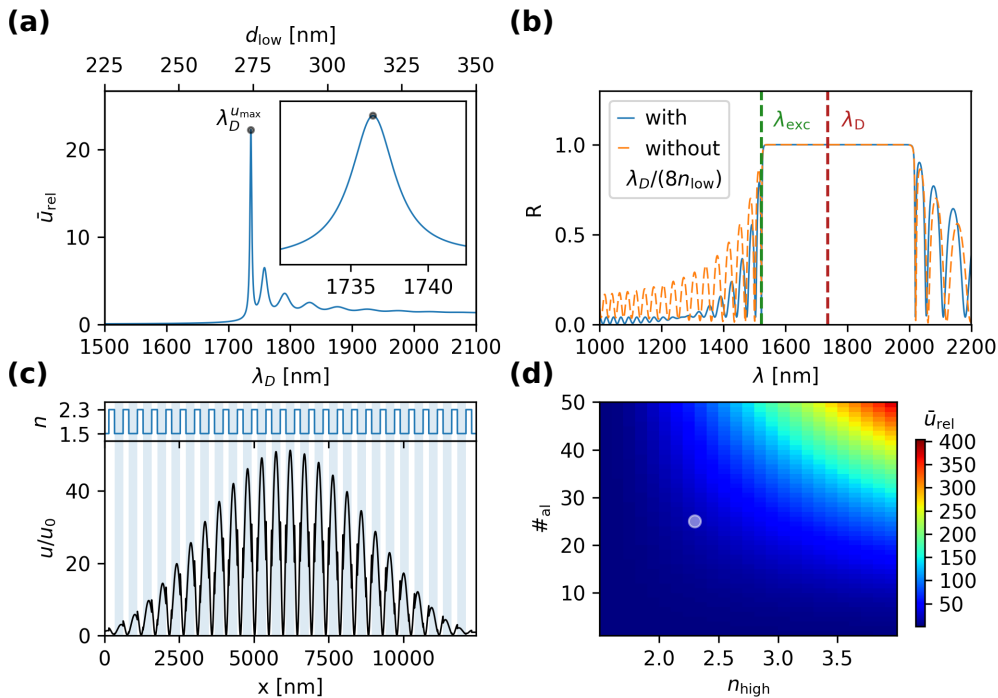


Fig. 3. (a) Average relative energy density \bar{u}_{rel} across the active layers as a function of design wavelength λ_D for an exemplary Bragg structure with $n_{\text{high}} = 2.3$ and $\#_{\text{al}} = 25$. The upper x -axis indicates the active layer thickness, $d_{\text{low}} = \lambda_D/(4n_{\text{low}})$. (b) Reflectance, R , for the example structure at the design wavelength yielding the maximum \bar{u}_{rel} -value, λ_D^{max} (marked by a black, shaded circle in panel a). (c) Spatial energy density distribution inside the structure for $\lambda_D = \lambda_D^{\text{max}}$. Additionally, the refractive index profile is shown. (d) Average relative energy density across the active layers as a function of n_{high} and $\#_{\text{al}}$. The example structure considered in panels a, b and c is marked by a white, shaded circle.

exemplary value of $n_{\text{high}} = 2.3$ was chosen in accordance with a recent experimental study where the high index layer was made of TiO_2 with $n = 2.3$ at 1523 nm [47]. The graph shows that for a certain design wavelength, λ_D^{max} , a very large enhancement of \bar{u}_{rel} occurs. As is known from the literature, a high field enhancement occurs at the photonic band edge [34, 65]. In Fig. 3(b), the reflectance for $\lambda_D = \lambda_D^{\text{max}}$ shows the position of the photonic band gap (PBG) relative to the excitation wavelength λ_{exc} . As expected, λ_{exc} lies close to the photonic band edge. In addition to the Bragg structure, the reflectance is also shown for a pure quarter-wave stack. Comparing the two curves, it is clear that the reduced thickness of the outer layers of the Bragg

structure causes a suppression of the side lobes of the reflectance peak. While this feature is not necessary for a perfect simulated structure under monochromatic excitation, it enables a more efficient in-coupling in experiments, in particular for broad-band excitation sources. The spatial dependence of u within the structure is illustrated in Fig. 3(c) for $\lambda_D = \lambda_D^{u_{\max}}$, along with the refractive index profile. A strong increase in u is observed inside the active layers of the structure. The enhancement can be explained in the context of photonic crystals as slow light piling up [66] or in a more classical context as the formation of a standing wave due to interference between the forward and backward propagating waves. It should also be noted that practically all energy density is located in the active layers.

Figure 3(d) shows \bar{u}_{rel} for the range of considered structures with $1.5 < n_{\text{high}} \leq 4.0$ and $1 \leq \#_{\text{al}} \leq 50$, evaluated at $\lambda_D = \lambda_D^{u_{\max}}$ for each structure. As the number of active layers and/or the refractive index contrast increases, the photonic effects become stronger and \bar{u}_{rel} increases. The associated increase in sharpness of the peak on the λ_D axis with respect to the layer thickness causes a correspondingly increasing sensitivity to structural imperfections. In fact, to obtain the maximum value of $\bar{u}_{\text{rel}} \approx 400$ shown in Fig. 3(d), the production accuracy must be subatomic. In this case, the peak of \bar{u}_{rel} on the λ_D axis reaches a sharpness in the sub-Ångström-range. Such accuracy can never be realized, and the extremely high \bar{u}_{rel} value is thus non-physical.

To take into account production tolerances, we apply a Monte Carlo method as described in section 2.1. The simulation results for four different σ -values are shown in Fig. 4. As can be seen,

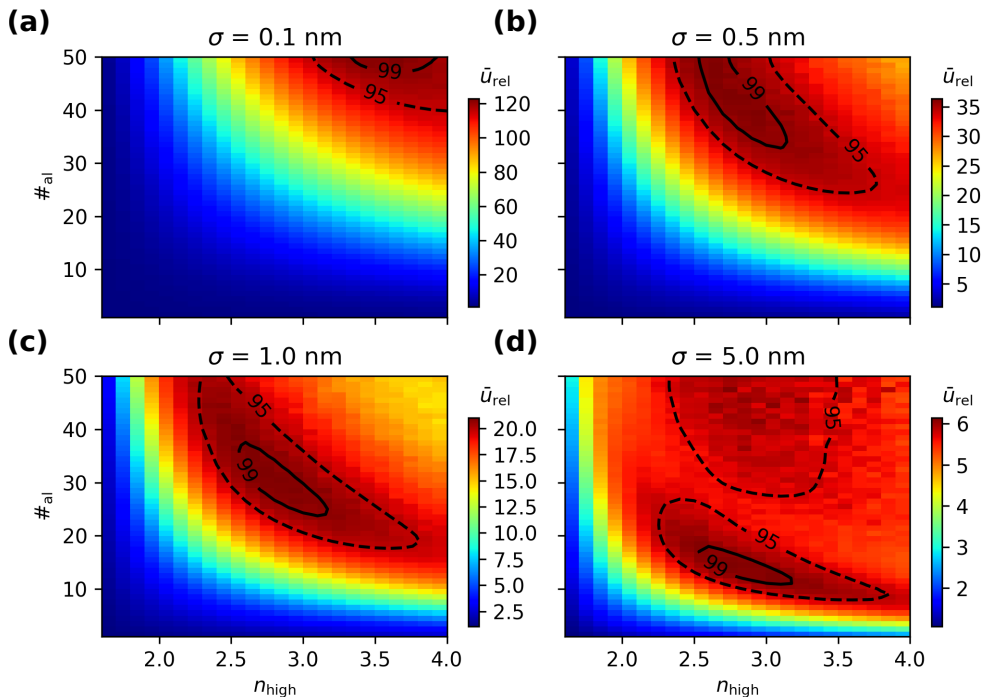


Fig. 4. Average relative energy density \bar{u}_{rel} across the active layers of a Bragg structure as a function of $\#_{\text{al}}$ and n_{high} . \bar{u}_{rel} is shown for four different production accuracies, simulated using a Monte Carlo method (see section 2.1). For each pixel, 50,000 separate calculations were carried out. The black contours indicate 99% (solid line) and 95% (dashed line) of the maximum. The panels show σ -values of 0.1 nm (a), 0.5 nm (b), 1.0 nm (c), and 5.0 nm (d).

the non-zero production tolerances limit the realistically achievable value of \bar{u}_{rel} severely. Even with Ångström precision, as displayed in Fig. 4(a), corresponding to the thickness of a single

atomic layer, the maximum value of \bar{u}_{rel} drops to around 125. With 0.5 nm and 1 nm precision, Figs. 4(b) and 4(c), the maximum decreases further to values around 35 and 20, respectively. Figure 5 shows the associated spread in u_{rel} for an exemplary $n_{\text{high}} = 2.3$. As more layers are

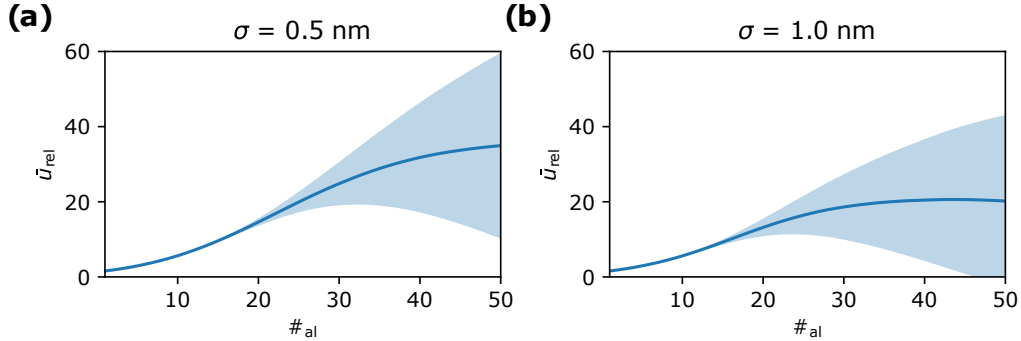


Fig. 5. Average relative energy density \bar{u}_{rel} across the active layers of a Bragg structure as a function of $\#_{\text{al}}$ for $n_{\text{high}} = 2.3$. \bar{u}_{rel} is shown for two different production accuracies, simulated using a Monte Carlo method (see section 2.1). For each data point, 50,000 separate calculations were carried out. The shadings indicate \pm one standard deviation. The panels show σ -values of 0.5 nm (a), and 1.0 nm (b).

added, the increasing sharpness of u_{rel} for the ideal structure causes a higher spread, which in turn lowers and broadens the mean-value maximum. The position of the mean-value maximum shifts towards structures with fewer layers, as exemplified in Fig. 5(b), and/or smaller refractive index contrast (see Fig. 4). As the peak in \bar{u}_{rel} for the ideal version of these structures is broader, they are less sensitive to structural imperfections compared to structures with more layers and/or a higher refractive index contrast. For $\sigma = 5$ nm, Fig. 4(d), the maximum moves further down, especially to lower $\#_{\text{al}}$, and the maximum value drops to around 6. Hence, to obtain high enhancement factors, high-precision manufacturing is of uttermost importance. Going forward, a production accuracy of $\sigma = 1$ nm is assumed, which is realistically attainable with current high-precision manufacturing methods.

3.2. Local density of optical states

The band structure and the relative local density of optical states (LDOS_{rel}) within the Wigner-Seitz unit cell is shown in Fig. 6 for two example structures with $n_{\text{high}} = 2.3$ (a) and $n_{\text{high}} = 3.0$ (b). Comparing the two structures, a compression of the band structure along the frequency axis when going from $n_{\text{high}} = 2.3$ to $n_{\text{high}} = 3.0$ is observed due to the increasing effective refractive index. In addition, the features become more pronounced and the size of the band gaps increases due to the increase in refractive index contrast. The LDOS influences the probability of all spontaneous emission processes (see section 2.3). In this work, the upconversion (UC) emission is almost exclusively caused by the spontaneous emission from energy level $3 \rightarrow 1$ (SPE31), while the radiative losses are dominated by the $2 \rightarrow 1$ emission (SPE21), see Fig. 2. To allow for a simple assessment of the LDOS effects of different structures, the ratio between the LDOS_{rel} for SPE31 and SPE21 is plotted in Fig. 7. Since, ideally, the UC emission should be enhanced and the loss emission suppressed, this ratio should be as high as possible. In Fig. 7(a), the LDOS_{rel} is plotted for an example structure with $n_{\text{high}} = 2.3$. The x -axis of Fig. 7 is λ_D , representing the scaling of the unit cell in position space. The orange and blue shaded regions indicate the position of the first photonic bandgap (1PBG) for SPE31 and SPE21, respectively. LDOS_{rel} is strongly reduced when the respective emission falls into the 1PBG. Therefore, the maximum ratio is observed when SPE21 is located in the region of the 1PBG, which is very close to λ_D^{umax} , the design wavelength that maximizes the relative energy density u_{rel} . It is important to note

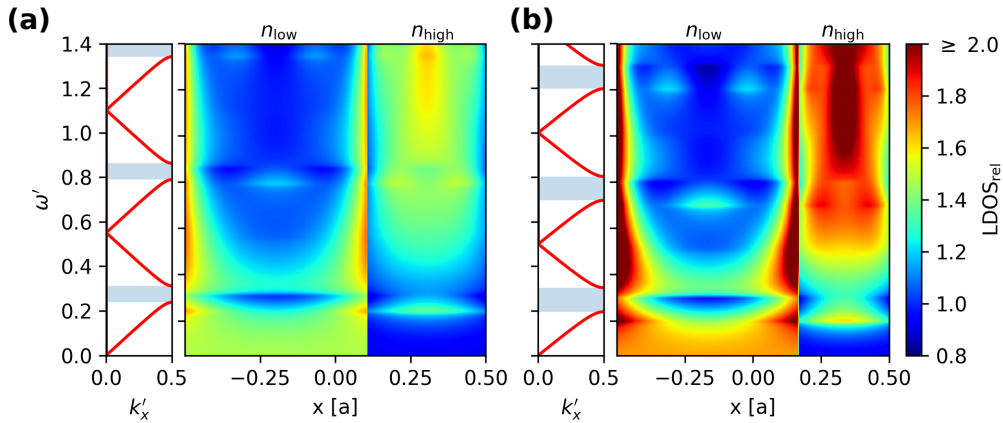


Fig. 6. Illustration of the LDOS for two different high index materials, $n_{\text{high}} = 2.3$ (a) and $n_{\text{high}} = 3.0$ (b), along with the associated photonic band structure for $k'_y = 0$. The regions of n_{high} and n_{low} (the active region) within the Wigner-Seitz unit cell are indicated on the top. The band gaps are marked by blue shadings. To avoid washing out features in the left panel, the scale is truncated at 2.0 even though the maximum value in the right panel is 2.5.

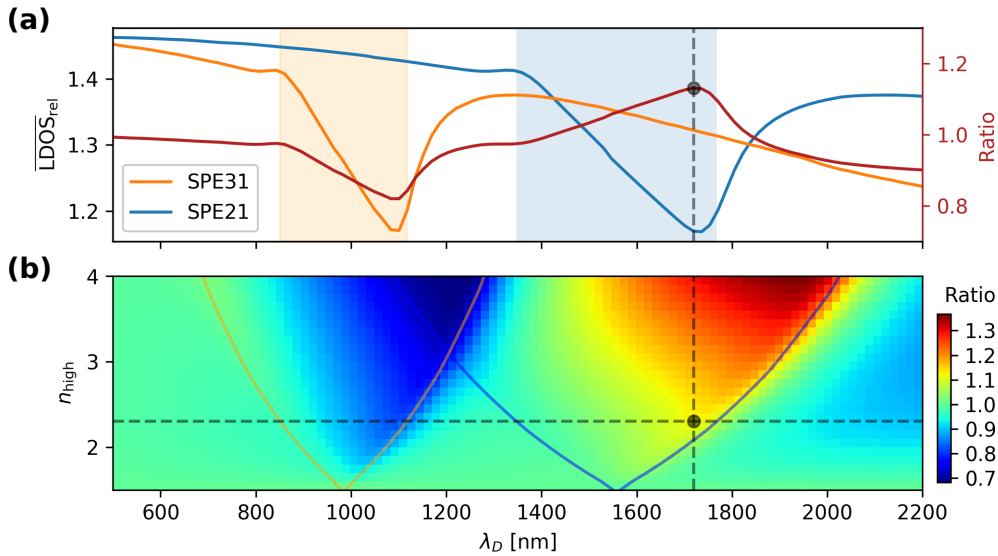


Fig. 7. (a) $\overline{\text{LDOS}}_{\text{rel}}$ for SPE31 (main UC emission) and SPE21 (loss emission), as well as their ratio for an example structure with $n_{\text{high}} = 2.3$ as a function of the design wavelength λ_D . The shaded regions indicate where the respective transition falls within the first photonic bandgap (1PBG). (b) Ratio of $\overline{\text{LDOS}}_{\text{rel}}$ for SPE31 and SPE21 as function of n_{high} and λ_D . The solid lines indicate where the respective transition falls within the 1PBG.

that the emission wavelength of 1558 nm is significantly stokes-shifted relative to the excitation wavelength $\lambda_{\text{exc}} = 1523$ nm. Therefore, λ_{exc} can be efficiently coupled into the structure at the edge of the 1PBG, while the emission wavelength is suppressed in the 1PBG.

In Fig. 7(b), n_{high} is varied on the y-axis. The grey dashed lines indicate the example structure shown in Fig. 7(a). The orange and blue lines indicate the edges of the 1PBG for SPE31 and

SPE21, respectively. For all n_{high} , the behavior is similar to Fig. 7(a). The ratio is small when the UC emission SPE31 falls into the 1PBG and large when the loss emission SPE21 lies in the region of maximum suppression in the 1PBG. Additionally, the ratio increases with increasing n_{high} . This can be understood from Fig. 6. As n_{high} increases, the features of the LDOS become more pronounced. Thereby, the contrast in the $\overline{\text{LDOS}}_{\text{rel}}$ increases between the region of the 1PBG and the band edges surrounding the 1PBG. We conclude that the most favorable design is obtained by placing SPE21 in the 1PBG while utilizing materials with the largest possible refractive index contrast.

3.3. Upconversion photoluminescence and quantum yield

Having analyzed the photonic effects of the local energy density enhancement and the local density of optical states (LDOS) separately, we now turn to their effect on UC as modeled using the rate equation model described in section 2.3. A detailed analysis of the photonic effects within the rate-equation-modeling framework, leading up to this work, can be found in [32]. In this section, we want to give an overview of the effects a Bragg structure can have on the upconversion quantum yield (UCQY) and upconversion photoluminescence (UCPL). To limit the analysis to physically realizable structures, a production accuracy of $\sigma = 1$ nm is assumed as discussed in section 3.1.

In Fig. 8, we illustrate the dependence of the UCQY on the incident irradiance. To limit the parameter space, we fix λ_D at $\lambda_D^{u_{\text{max}}}$, the design wavelength where the enhancement of the energy density is at its maximum. For low irradiances, this is a reasonable approximation, as the energy density enhancement is the most important effect in this regime. Additionally, as discussed in sections 3.1 and 3.2, $\lambda_D^{u_{\text{max}}}$ is typically close to the λ_D for which the benefit of the LDOS, i.e. the ratio between $\overline{\text{LDOS}}_{\text{rel}}$ for SPE31 and SPE21, is at its maximum. Since the peak of this ratio in λ_D space is much broader than that of \bar{u}_{rel} , $\lambda_D^{u_{\text{max}}}$ will typically yield a UCQY value close to the maximum possible value.

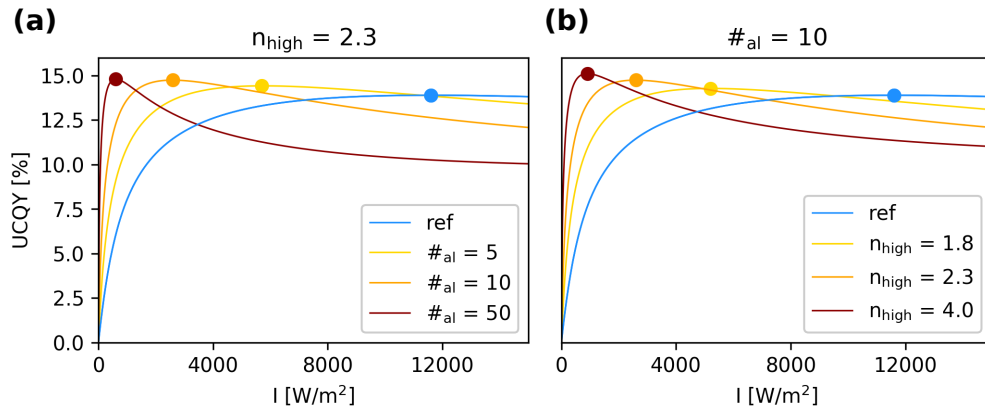


Fig. 8. UCQY as a function of incident irradiance I for exemplary families of Bragg structures with (a) n_{high} fixed at 2.3 while $\#_{\text{al}}$ is varied and (b) $\#_{\text{al}}$ fixed at 10 while n_{high} is varied. In both cases $\lambda_D = \lambda_D^{u_{\text{max}}}$. For the Bragg structures, higher UCQY values at much lower irradiances are achievable. The maximum for each design is marked with a large dot.

In Fig. 8(a), we fix n_{high} at 2.3 and vary only the number of active layers, $\#_{\text{al}}$. This allows studying the effect of \bar{u}_{rel} , as the calculated LDOS varies only slightly with $\#_{\text{al}}$ (due to the change in $\lambda_D^{u_{\text{max}}}$). To reach the maximum UCQY for the reference, an irradiance of 11600 W/m^2 is needed. This optimal irradiance is characteristic for the regarded material system. At higher

irradiances, the population of higher energy levels becomes more dominant, such that the UCQY decreases. For the Bragg structures, the UCQY curve is compressed along the irradiance axis, i.e. a lower incident irradiance is needed to achieve the optimal irradiance at the position of the upconverter. From Fig. 4(c) we know that for $n_{\text{high}} = 2.3$, \bar{u}_{rel} increases with increasing $\#_{\text{al}}$. Therefore, the compression of the UCQY curve on the irradiance axis is stronger for higher $\#_{\text{al}}$. Additionally, the maxima for the Bragg structures are slightly higher than for the reference due to the modified LDOS. For additional discussion on this point, we refer to [32]. In Fig. 8(b), $\#_{\text{al}}$ is fixed at 10 while n_{high} is varied. From Fig. 4(c) we know that at $\#_{\text{al}} = 10$, \bar{u}_{rel} increases with increasing n_{high} . That is, as the refractive index contrast increases, fewer layers are needed to reach the same energy density enhancement. Similar to the case of increasing $\#_{\text{al}}$, a compression along the irradiance axis occurs. Additionally, the Bragg structure maximum point goes to higher UCQY values with increasing n_{high} due to the increasing strength of the LDOS modification as illustrated in Figs. 6 and 7.

To enable an assessment of structural designs in two dimensions, we reduce the dimensionality of the parameter space by fixing the irradiance at specific application scenarios. For non-concentrated sunlight, the irradiance available from the air-mass 1.5 global spectrum within the absorption range of Er^{3+} (from 1450 nm to 1600 nm) is approximately 30 W/m^2 [19]. A higher incident irradiance case of 1000 W/m^2 could be reached by combined spectral and geometrical concentration [67]. To also investigate the photonic upconverter system in the high irradiance regime, we regard the case of 10000 W/m^2 (1 W/cm^2).

For each scenario, the UCQY is shown as a function of n_{high} and $\#_{\text{al}}$ in the left panels of Fig. 9. In the first panel, $I = 30 \text{ W/m}^2$, the incident irradiance is so low, that the UCQY is determined almost exclusively by the energy density enhancement. This explains the structural resemblance of Fig. 9(a) to Fig. 4(c). The highest UCQY reached for this irradiance is 6.7%. At $I = 1000 \text{ W/m}^2$, Fig. 9(c), UCQY values up to 15.4% become possible. With $n_{\text{high}} = 2.3$, 95% of this maximum value can be reached with 20 layers, while for $n_{\text{high}} = 3.0$ only 10 layers are needed. Because of the saturation of the UCQY that is clearly visible in Fig. 8 for the reference, the UCQY does not feature a strong dependence on the irradiance. Hence, the observed maximum of the UCQY is rather broad. Going to even higher irradiances, Fig. 9(e), saturation occurs and the UCQY starts decreasing (see also Fig. 8). Hence, in concentrated-solar applications, the benefit of the Bragg structure decreases regarding the UCQY. However, it should be noted that higher UCQY values than shown are possible by tuning the design wavelength. In the case of a very high incident irradiance, the assumption of $\lambda_D = \lambda_D^{\text{max}}$ being an almost-ideal choice for maximizing the UCQY, is no longer valid.

For some applications, the UCPL is of more interest than the UCQY. Therefore, we also investigate the relative UCPL (UCPL_{rel}) as shown in the right panels of Fig. 9, again as a function of n_{high} and $\#_{\text{al}}$. While the absorption enhancement is directly given by the energy density enhancement, the UCPL depends non-linearly on the local energy density. This non-linearity saturates to linearity at a characteristic irradiance threshold. Therefore, at low irradiances far from saturation, the UCPL can be increased by orders of magnitude compared to the performance of the reference. For the very low irradiance of $I = 30 \text{ W/m}^2$, Fig. 9(b), the Bragg structure enables a 330-fold UCPL enhancement. At $I = 1000 \text{ W/m}^2$, Fig. 9(d), the maximum UCPL enhancement has decreased to ≈ 40 -fold. At this irradiance the relative effect of the Bragg structure is lower because the UCQY of the reference is already much higher. Proceeding to the case of $I = 10000 \text{ W/m}^2$ (1 W/cm^2) plotted in Fig. 9(f), the enhancement factor drops further to a maximum of ≈ 12 . At this high irradiance, the UCQY is in fact lower for some Bragg structures compared to the reference, which causes the UCPL enhancement to drop below the energy density enhancement. In consequence, the ideal design for the UCPL enhancement is a different one than for the UCQY enhancement.

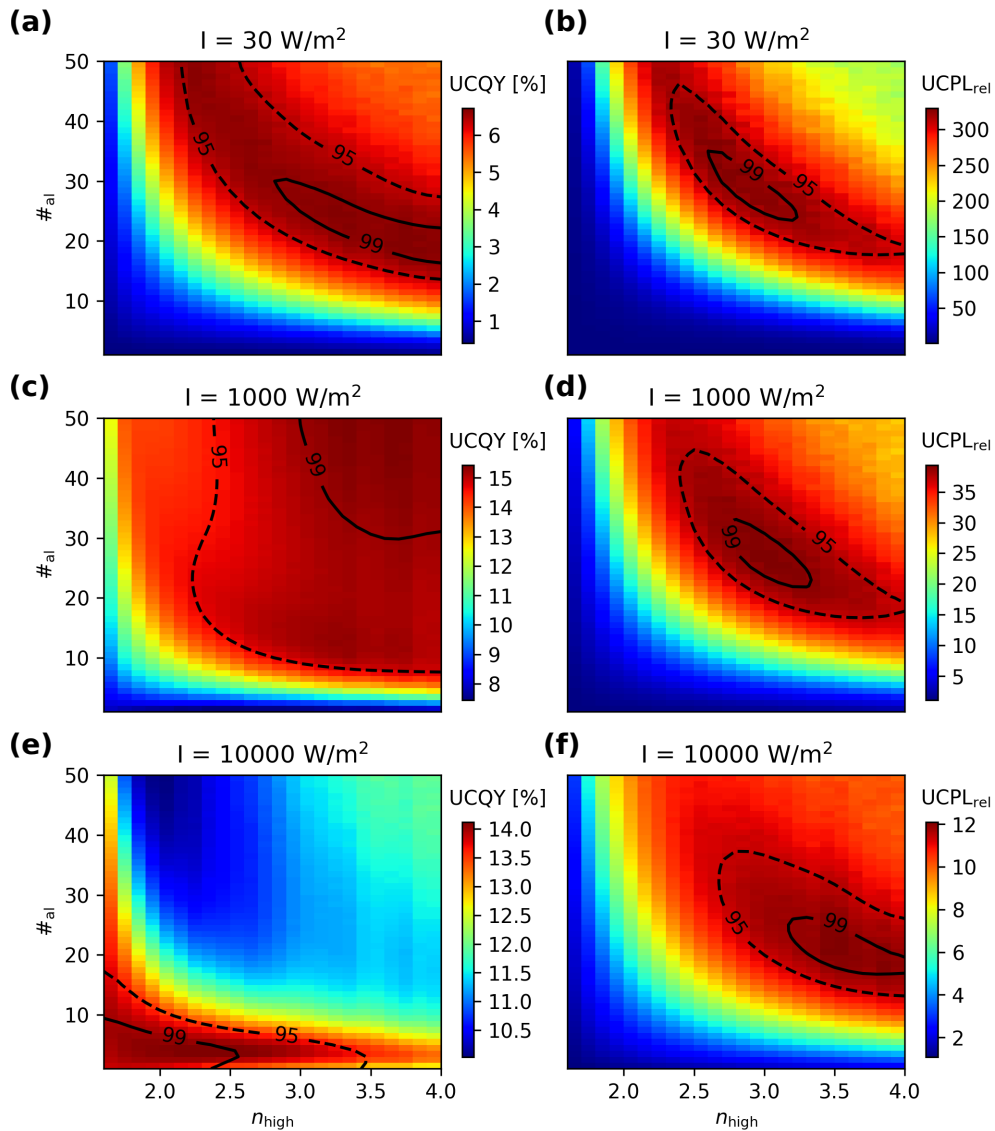


Fig. 9. UCQY (left) and relative UCPL (right) as a function of n_{high} and $\#_{\text{al}}$ for $\lambda_D = \lambda_D^{u_{\text{max}}}$. The black contour lines indicate 99% (solid line) and 95% (dashed line) of the maximum in each plot. The rows show different irradiance scenarios of $I = 30 \text{ W/m}^2$, 1000 W/m^2 , and 10000 W/m^2 (1 W/cm^2).

3.4. Discussion of results

Experimental work on erbium-doped distributed Bragg reflectors has previously been published by Johnson *et al.* [34]. Their structures were made of Er^{3+} -doped porous silicon, where the periodic variation of the refractive index was achieved by varying the silicon porosity. At an excitation wavelength of 1550 nm and a laser power of 200 mW, an UCPL enhancement of 26.6 is reported for the 550 nm UC emission. The main UC emission of 980 nm was enhanced by a factor of around 5. The investigated structure by Johnson *et al.* corresponds to our simulated Bragg structure of $\#_{\text{al}} = 30$, featuring refractive indices of $n_{\text{low}} \approx 1.5$ and $n_{\text{high}} \approx 2.2$. Johnson *et*

al. report difficulties in controlling the layer thickness accuracy in the structures, hence we draw a comparison to our lowest simulated accuracy. Johnson *et al.* do not report the exact irradiance, but that the 200 mW laser beam is focused on the sample. Therefore a high irradiance can be assumed and we draw a comparison to our highest simulated irradiance. At a production accuracy of $\sigma = 5$ nm and an irradiance of 10000 W/m^2 , we calculated an UCPL enhancement of 4.8. This is very well in line with the measured enhancement of a factor of 5 by Johnson *et al.*, especially, when taking into account the complexity of both the simulation model and the experiment.

Works on other photonic structures are not directly comparable. Nevertheless, it is possible to draw a comparison in terms of advantages and disadvantages of the different structures. In a waveguide structure a very high enhancement of 10^4 has been reported by Lin *et al.* [43]. The downside of this very effective device, at least in application in photovoltaics, is that the enhancement occurs only within a very narrow range in excitation wavelength and incident angle (approximately 1 degree). Opal photonic crystal structures often exploit surface effects, which allow only for a thin layer of upconverter material to be deposited on top of the photonic structure. This limits the amount of upconverter material affected by the enhancement and therefore the total UC signal. Enhancement factors of up to 30 have been reported by Niu *et al.* [38] and Yin *et al.* [36]. Later, Yin *et al.* also included gold nanorods in opal photonic crystal structures to additionally exploit plasmonic effects, raising the UC enhancement factor to three orders of magnitude [44]. In inverse opal photonic crystal structures, the voids of the structure can be filled with UC material, allowing for more upconverter material to be included in the device [37, 40]. Here, the performance of the structures deviates by an order of magnitude with Zhang *et al.* measuring a maximum UC enhancement factor of 4.6 [40], while Xu *et al.* report a factor of 43 [37]. Recently Shao *et al.* demonstrated the additional usage of plasmonic effects, embedding gold nanoparticles in inverse opal photonic structures. With a measured UC enhancement factor of 10 [45], no clear benefit compared to pure photonic structures was observed. In comparison to all these reported structures, the Bragg structure is a promising device. The amount of upconverter material affected by the enhancement can be varied, and indeed can be quite large. Simultaneously, high UCPL enhancement factors can be reached.

Other factors that will affect the applicability of any photonic structure, especially in photovoltaics, is its sensitivity to spectral and/or angular changes of the excitation, as well as the angular characteristics of the emission. Investigating these dependencies is beyond the scope of this paper, but the topics will be addressed in our future work.

4. Summary

We have presented a simulation-based analysis of the photonic effects of a Bragg structure on the upconversion quantum yield (UCQY) and the upconversion photoluminescence (UCPL) of the embedded upconverter, $\beta\text{-NaYF}_4\text{:Er}^{3+}$. The change in local energy density and the local density of optical states were considered within a rate-equation-modeling framework. To include all realistically attainable structures in the analysis, the refractive index of the spacer material, n_{high} , was varied within the refractive index range of naturally occurring materials, $1.5 < n_{\text{high}} \leq 4.0$, and up to 50 active layers were considered. Furthermore, manufacturing imperfections were incorporated in the analysis via Monte Carlo simulations.

Neglecting production imperfections, the energy density across the active layers of the Bragg structure can be enhanced indefinitely, simply by adding more layers. For 50 layers, a more than 400-fold average enhancement was found for $n_{\text{high}} = 4.0$. However, when realistic production accuracies are taken into account, the maximum shifts to fewer layers and takes on a finite value. At $\sigma = 1$ nm and $\sigma = 5$ nm, for example, the enhancement drops to 20- and 6-fold, and the number of active layers needed are only 30 and 15, respectively. These observations underline the crucial importance for high-precision manufacturing methods in order to realize efficient Bragg structures experimentally. Furthermore, we showed that for all applications it is highly

profitable to use the maximum possible refractive index for the spacer layer. The higher refractive index contrast significantly increases the beneficial photonic effects. Additionally, it decreases the number of layers needed to reach a given energy density enhancement, which decreases the complexity of the fabrication process.

For an optimized Bragg structure, a 330-fold UCPL enhancement was predicted at an illumination of one sun for a production accuracy of $\sigma = 1$ nm. However, due to a non-ideal effective energy density, the UCQY remains below 7%. At an incident irradiance equivalent to 30 suns, possible e.g. using a combination of down-shifting and geometrical concentration [67], the UCQY of the optimized Bragg structure is raised to a near-maximum value of 15.4%, while the reference remains at only 8.0%.

In conclusion, we find that the Bragg structure is a very promising candidate for increasing the efficiency of upconversion processes in a broad range of applications. In particular within the context of non-concentrated photovoltaics, the combination of a high UCPL enhancement and the possibility of including a large amount of upconverting material makes the Bragg structure exceedingly favorable.

Funding

Baden-Württemberg Ministry of Science, Research and Arts; Baden-Württemberg Ministry of Finance and Economy; Sustainability Center Freiburg under the NaLuWiLeS project; Innovation Fund Denmark under the SunTune project; Heinrich-Böll Stiftung; Helmholtz Association under the STN research program.